Highlighting the role of heterogeneity on the indentation hardness of foamed gypsum

Julie Devillard, Jerome Adrien, Stéphane Roux, Sylvain Meille, Éric Maire

Version of Record: https://www.sciencedirect.com/science/article/pii/S0955221920300893
Manuscript_fd0d6f4a802a41edd0fcbb22d2522386

Highlighting the role of heterogeneity on the indentation hardness of foamed gypsum

Julie Devillard[1], Jérôme Adrien[1], Stéphane Roux[2], Sylvain Meille[1], and Eric Maire[1]

[1]Université de Lyon, INSA-Lyon, MATEIS, CNRS UMR5510, F-69621 Villeurbanne, France
[2]LMT, ENS Paris-Saclay / CNRS / Université Paris-Saclay, Cachan, France

January 22, 2020

Abstract

The objective of this work is to link microstructure features of foamed gypsum (lightweight gypsum board core material) and its compressive properties. Several samples of foamed gypsum with different microstructures were manufactured and characterized by X-ray tomography and 3D image processing. Spherical indentation tests results show that for a similar density, the size distribution of the macropores and the distribution of the three levels of porosity has only a very small influence on the mechanical properties. In contrast, the density and homogeneity of spatial distribution of macropores has a much stronger impact on hardness.

Keywords: Lightweight plasterboards, spherical indentation, X-Ray tomography, image processing, porosity, homogeneity, microstructure

1 Introduction

Plasterboards are commonly used in construction since their invention in 1894 by A. Sackett. Their properties in terms of fire resistance and acoustic insulation provide a low-cost solution for the building industry. In order to improve their performance, the influence of gypsum microstructure on mechanical properties [1–5] as well as on its fire resistance [6, 7] has been studied. Industry is interested in enhancing or at least preserving these properties while reaching lower densities. A decrease in plasterboard weight leads directly to production, transportation and environmental costs savings.

However, plasterboards lightening often leads to the degradation of mechanical properties and plasterboards have to fulfill standard requirements to be placed on the market. One of these tested properties is the nail pull strength [8]. Nail pull test helps quantifying the resistance of plasterboard to perforation and it is one of the most severe requirement for lightweight plasterboards. A lightweight plasterboard is made of a core material which is foamed gypsum, a layer of dense gypsum called "roller coating" and paper (see Figure 1a). During perforation of the plasterboard, it has been observed that crushing of the core material is the limiting mechanism for failure [9]. This study will thus focus on the core material compression properties.

Foamed gypsum is usually obtained by mixing the plaster slurry with foam (made of liquid foaming agent, air and water). If the microstructure of gypsum and foam is well known separately, interactions occur during the formulation process and impact the final microstructure. X-Ray computed micro-tomography is an appropriate technique to inspect the 3D microstructure of foamed gypsum in a non-destructive way because of the high porosity fraction of foamed gypsum [11]. Foamed gypsum is indeed a material containing porosity at three scales. At the macroscopic scale, large spherical pores (with an equivalent diameter larger than 100 μm) are due to the addition of foam into the gypsum (Fig. 1b). At smaller mesoscopic scale the gypsum contains mesopores[1] (Fig. 1c). These are due to the dissolution of the largest semi-hydrate particles during gypsum hydration, their size and shape are then related to the initial plaster powder's granulometry [10]. At the small microscopic scale, gypsum contains a percolating network of small pores left between the gypsum needles (Fig. 1d). In this study, we consider that the limit between mesopores and micropores is around 10 μm. This practically corresponds in our case to the smallest detectable mesopores at the resolution typically used for tomographic scans.

The nail pull test is critical for lightweight plasterboards and during this test, the core material is mostly loaded locally in compression [9]. Spherical indentation seems to be appropriate to reproduce the strain state during a nail pull test because it is easy to run and it induces stress in the material at a scale comparable to that of nail-pull. Our objective in this paper is to characterize the indentation response of foamed gypsum in a broad range of porosity distribution and to link the hardness to the microstructure. We will discuss the effect of macropores size, fraction and spatial distribution on the mechanical properties of foamed gypsum.

[1]Here we do not follow the IUPAC nomemclature: "A mesoporous material is a material containing pores with diameters between 2 and 50 nm, according to IUPAC nomenclature. For comparison, IUPAC defines microporous material as a material having pores smaller than 2 nm in diameter and macroporous material as a material having pores larger than 50 nm in diameter."

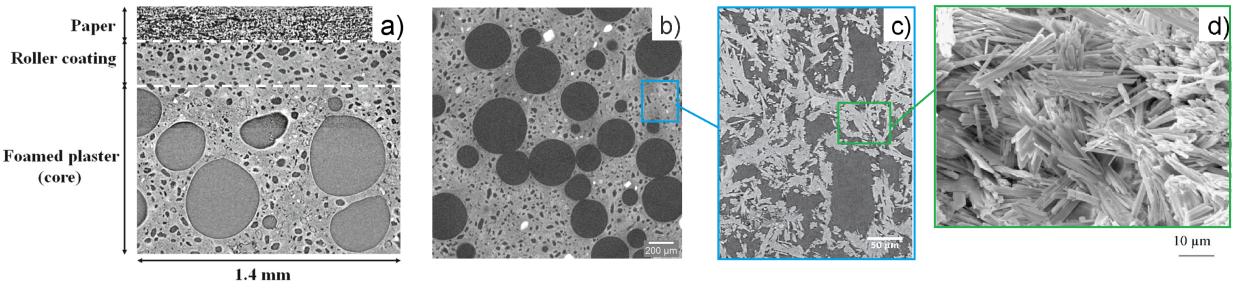

Figure 1: *a) lightweight plasterboard structure: paper, roller coating and foamed plaster [9] b) macroporosity of foamed gypsum (large spherical pores) on a X-ray tomography scan with a 2 μm voxel size c) mesoporosity due to hemihydrate dissolution on a tomography scan [10] d) SEM image of microporosity between entangled gypsum crystals [3]*

2 Materials and methods

2.1 Sample preparation

Different formulations of foamed gypsum were used for this study. Samples were prepared from synthetic plaster (Desulphogypsum or DSG). A reference grade was prepared with water, plaster powder, foam and basic additives: accelerator, set retardant, starch and thinning agent according to the composition listed in Table 1. The water/plaster ratio was set at 0.7, taking into account the water provided by the foam.

Table 1: *Formulation of reference grade*

Component	Set retardant	Accelerator	Thinning agent	Starch
Percentage of plaster mass	0.10%	0.50%	0.13%	0.50%

Foamed gypsum can be obtained by using chemical additives in order to form gas bubbles or by means of air entrainment in wet gypsum slurry [12, 13]. To produce the samples in our study, we used another method where the plaster slurry was mixed with foam. This foam was produced with a foam generator from air, water and surfactant. This method allows us to better control the macroporosity microstructure. Lower densities can also be reached.

In a first step, the plaster was slowly added into the water and additives during 30 s. This slurry was mixed at low speed during 30 additional seconds until complete wetting of the powder. Then the slurry was mixed at high speed. Foam was added into the slurry while stirring at low speed with a rectangular blade. To ensure good dispersion of the foam in the slurry, the mixing was pursued manually for 40 additional seconds. The foamed slurry was then cast into silicone molds to prepare 10 cm$\times$2 cm$\times$2 cm bars. The typical setting time was about 10 min. After 30 min the hydration was complete, samples were removed from the molds and dried for at least 24 hours at 40°C in dry atmosphere.

In order to explore different microstructures, for each formulation three parameters were independently varied: density, water-plaster ratio and type of the foam generator as shown in Table 2. The obtained microstructures are illustrated in Figure 2. For the different formulations, only the thinning agent amount was adjusted to control the rheology of the slurry. A similar rheology was targeted for each formulation in order to compare the resulting dry samples mechanically. It is important to note that the use of a thinning agent leads to destabilization and drainage of foam bubbles. The higher the fraction of the thinning agent, the larger the size of the bubbles. These bubbles appear mostly at the upper surface of the sample. For a formulation with a smaller water/plaster ratio, more thinning agent would be needed and so the slurry may have larger defects.

The parameter having the major impact on the mechanical properties is likely to be the density. To change density, the amount of foam was varied and W70, W75, W80, W90 and W100 formulations were obtained (cf. Table 2). The overall density (ρ) was calculated based on the mass and volume of the samples with respect to that of fully dense gypsum ($\rho_{dense} = 2.32\ \mathrm{g/cm^3}$). The samples did not have perfectly regular dimensions, so the sizes of the dried samples were measured at several locations. The standard deviation of volume measurement was estimated to be 1.2% and this led to an error on the measured density of $\pm 1.2\%$ (the uncertainty in the mass measurement being less than 0.01%).

The distribution of the three levels of porosity can also be modified for a given density. To do so, the water/plaster ratio was changed to obtain R06 and R08 formulations (cf. Table 2). This ratio takes into account the water in the slurry but also the water coming from the foam. So by decreasing water/plaster ratio, with the same overall density, we had to increase the amount of foam and decrease the amount of water in the slurry.

Another way of changing the porosity distribution is to change the foam generator. Two types of foam generator were used: type 1 for the REF formulation and type 2 for the DG formulation (cf . Table 2). The type 2 foam generator is expected to produce smaller bubbles than type 1. For both generators, the liquid flow was set to around 3.25 $\mathrm{cm^3/s}$ with a peristaltic pump and the air flow was adjusted to produce foam with a targeted density of 91 kg/$\mathrm{m^3}$.

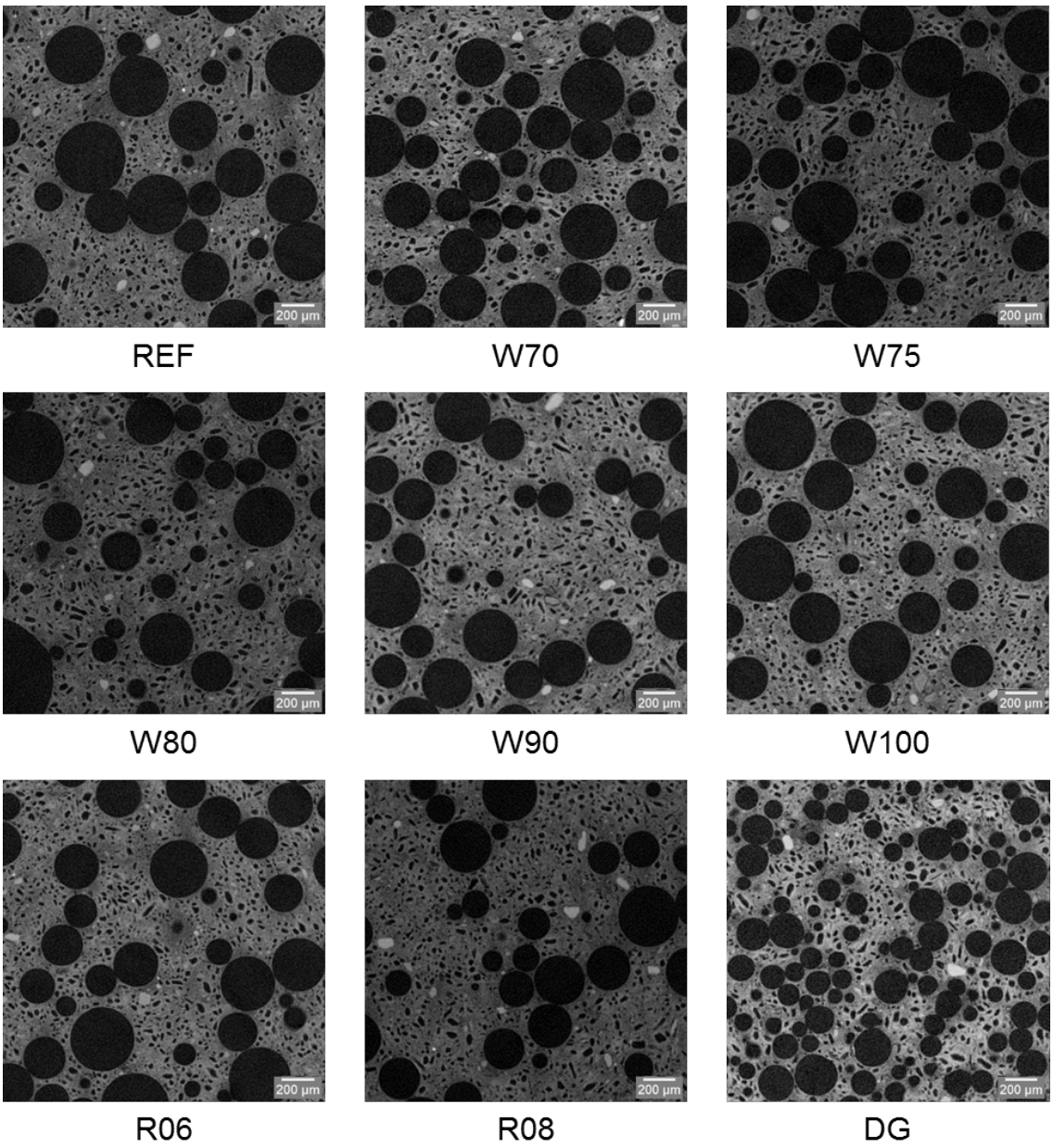

Figure 2: *Slice of tomography scan with a voxel size of 2 μm for the 9 foamed gypsum formulations*

Table 2: *Features of the 9 formulations used in this study. Varying parameters compared to the reference are indicated in gray.*

Designation	Board Weight	Water/Plaster Ratio	Foam generator
REF	8.5 $\mathrm{kg/m^2}$	0.7	Type 1
W70	7.0 $\mathrm{kg/m^2}$	0.7	Type 1
W75	7.5 $\mathrm{kg/m^2}$	0.7	Type 1
W80	8.0 $\mathrm{kg/m^2}$	0.7	Type 1
W90	9.0 $\mathrm{kg/m^2}$	0.7	Type 1
W100	10.0 $\mathrm{kg/m^2}$	0.7	Type 1
R06	8.5 $\mathrm{kg/m^2}$	0.6	Type 1
R08	8.5 $\mathrm{kg/m^2}$	0.8	Type 1
DG	8.5 $\mathrm{kg/m^2}$	0.7	Type 2

2.2 Microstructure Characterization

2.2.1 X-ray tomography

X-ray tomography was used to perform 3D analysis of the internal microstructure of foamed gypsum samples. Scans were carried out using a Vtome|X device (GE Phoenix, X-Ray GmbH). This tomograph is equipped with a 160 kV nano-focus tube, a tungsten transmitting target, and a 1920×1536 pixel Varian detector (see [14] for more details). The X-ray tube produces a polychromatic conical beam. The scans were performed at a voltage of 80 kV and a current of 280 μA, with a voxel size of 2 μm, 5 μm or 15 μm. 3D volumes were reconstructed using the GE phoenix datos|X CT software. Reconstructed scans were processed using the Fiji free software [15].

2.2.2 Thresholding of porosity

For the 15 μm voxel size scans, thresholding was rather straightforward because at this resolution, only the macropores can be identified. A simple automatic threshold according to the Li method [16] based in the minimum cross-entropy of the gray level histogram, was used on these low resolution volumes.

For the 2 μm and 5 μm scans, thresholding turned out to be more complex. The presence of two porosity scales (macropores and mesopores) is indeed an issue. In order to threshold the macropores, the same Li method was used. However, even if the bubbles were correctly thresholded, the mesopores size and fraction were clearly under-estimated. The gray level variation of the gypsum phase does not allow a global threshold calculation. Thus, an auto local threshold technique according to the method of Phansalkar [17] was used to binarize mesopores. After this step, the description of macropores was however not completely satisfactory because of the noise present inside the large pores. To reach a better segmentation of both the macro and the meso porosity, these two binary volumes were combined with a logical operation AND applied on the binary images (the obtained solid phase was set prior to the logical combination). Each voxel was considered as belonging to the gypsum phase if and only if both procedures gave a positive answer. The method principle is illustrated using one tomographic slice in Figure 3.

The quality of this thresholding method was visually verified using the method shown in Figure 4. This method consists of recovering only the contours of the thresholded image and superimposing them with the original gray scale image. This verification technique confirms the quality of the thresholding because the contours describe satisfactorily the pores that are visible at this resolution.

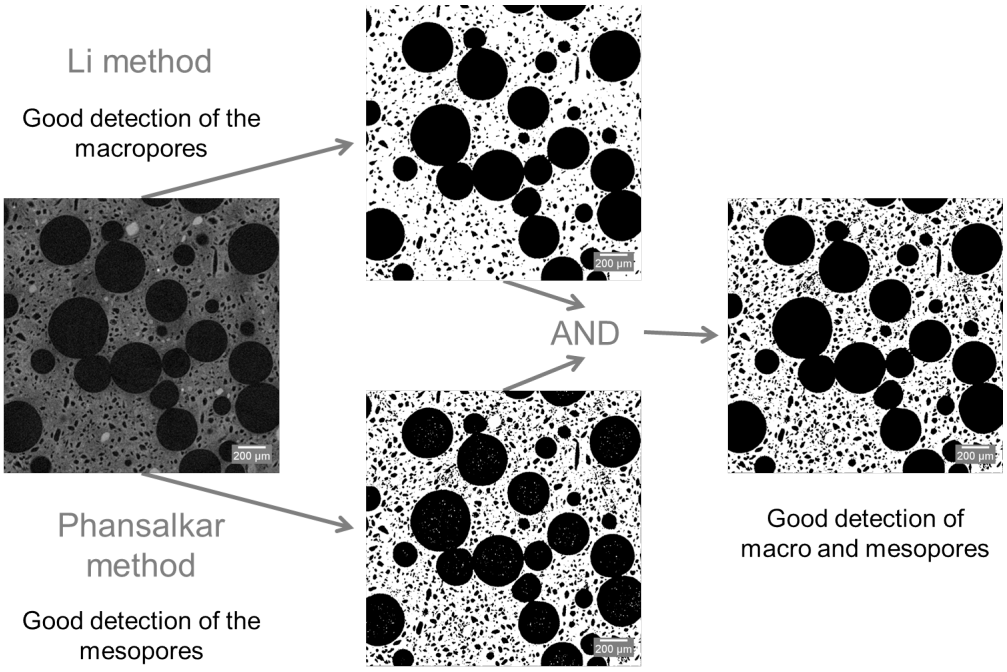

Figure 3: *Image processing to threshold porosity on 2 µm voxel size tomography scans*

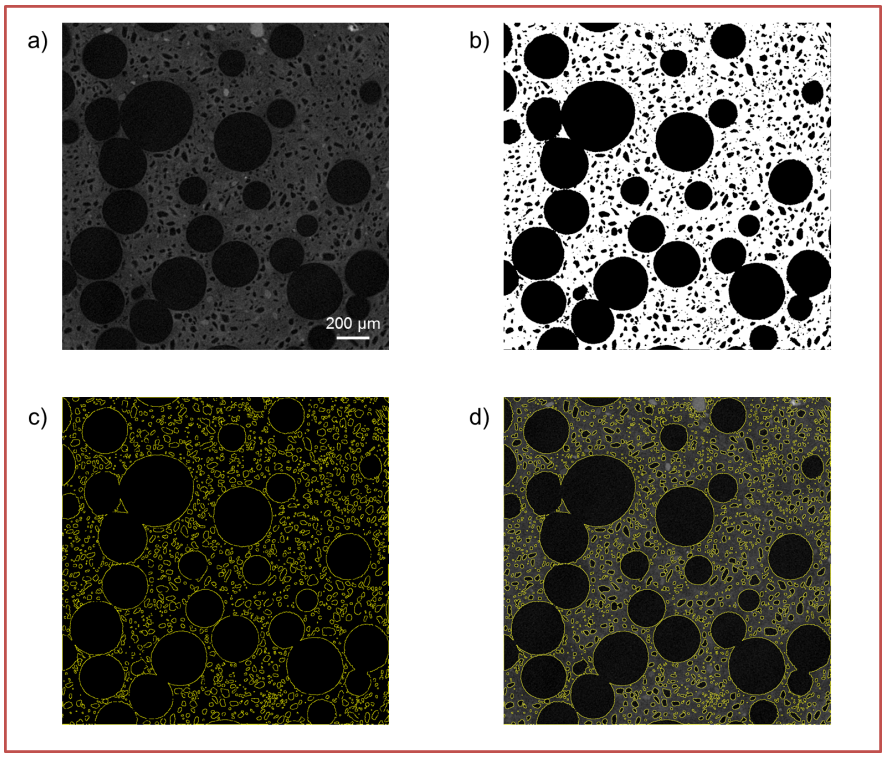

Figure 4: *Method to control the quality of the thresholding a) slice of a gray level volume b) slice after thresholding c) contours of the thresholded porosity d) contours superimposed on the original gray level image*

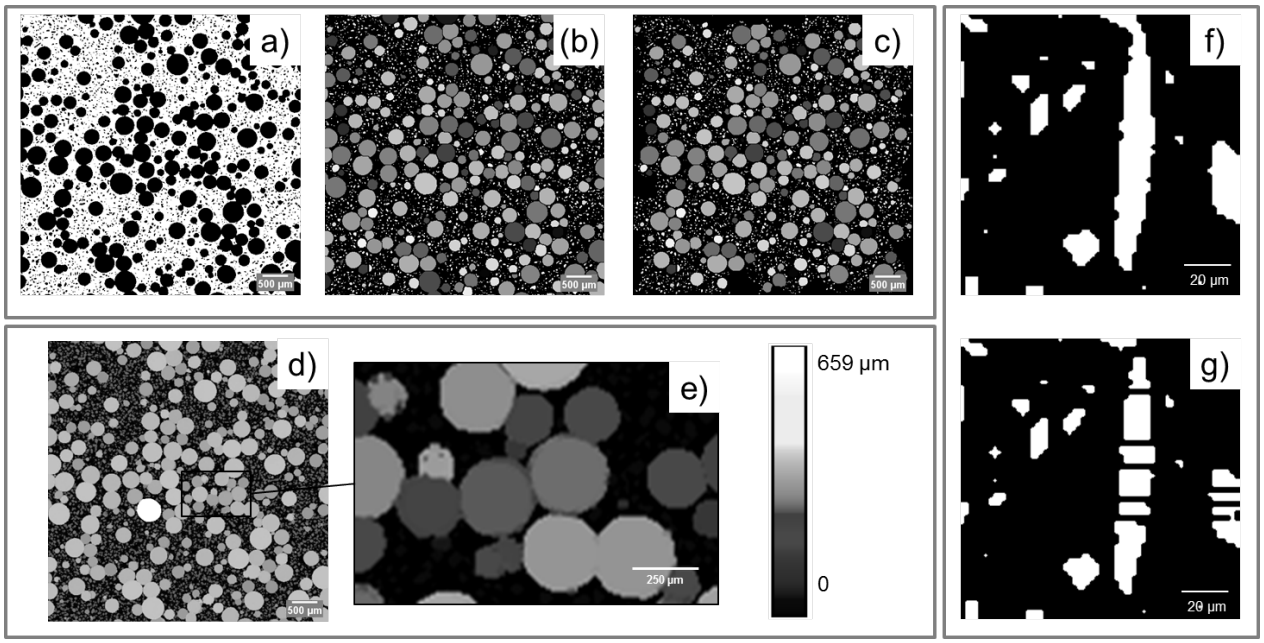

Figure 5: *Image processing to calculate size distribution of porosity. For macropores, with watershed method: (a) slice of a thresholded volume with 5 μm voxel size, (b) separated and labeled pores after watershed processing, (c) separated and labelled pores without the bordering ones ; with the morphological method: (d) 3D-granulometry map, (e) zoom on non-spherical pores. For mesopores: (f) thresholded mesopore, (g) after watershed processing*

2.2.3 Size distribution measurement of porosity

Macropores distribution was determined from volume analysis on the 5 μm voxel size scans. Two methods available to measure the size distribution of the porosity were compared. The first one consists in splitting coalesced macropores using a conventional watershed algorithm [18, 19]. This was practically achieved here by using the "3D Watershed Split" plug-in in Fiji [20] and pores were subsequently labeled. The volume of each macropore was then measured (by voxel counting of each label) and their equivalent diameter (representing the diameter of the sphere having the same volume as the pore) was calculated. If a pore happens to be in contact with at least one edge of the volume, it is likely to be truncated. As a consequence, each pore touching the edges was removed before computing the size distribution. The method's principle is summarized in the Figures 5a, b and c. From these data, it was possible to get the size distribution of the macro-porosity.

A morphological method named 3D-granulometry can also be used to measure the size distribution of a phase in a reconstructed volume. In our case we used the Local Thickness Fiji plug-in [21] in order to determine the thickness distribution of the pores. The algorithm finds the biggest sphere fitting each region of the considered phase and the voxel's value in the region is set to the diameter of this sphere (Fig. 5d). Macropores are not perfectly spherical and hence at their periphery some of their voxels inevitably do not have the same value after such a 3D-granulometry measurement as shown in Figure 5e. This leads to underestimating the amount of large pores.

These two methods were compared for the size distribution of the macropores of the reference formulation. The results of the two methods are plotted in Figure 6. The size distributions are observed to be rather close but — as expected— slightly shifted to smaller values for the morphological method. For the size measurement of macropores, the watershed method was finally selected.

On the contrary, the watershed method is not really suited for measuring the size of the mesopores as it tends to erroneously split the most elongated mesopores into two or more smaller pores (Fig. 5f and g). For measuring the thickness distribution of the mesopores, the 3D-granulometry method was thus applied on the 2 μm voxel size scans.

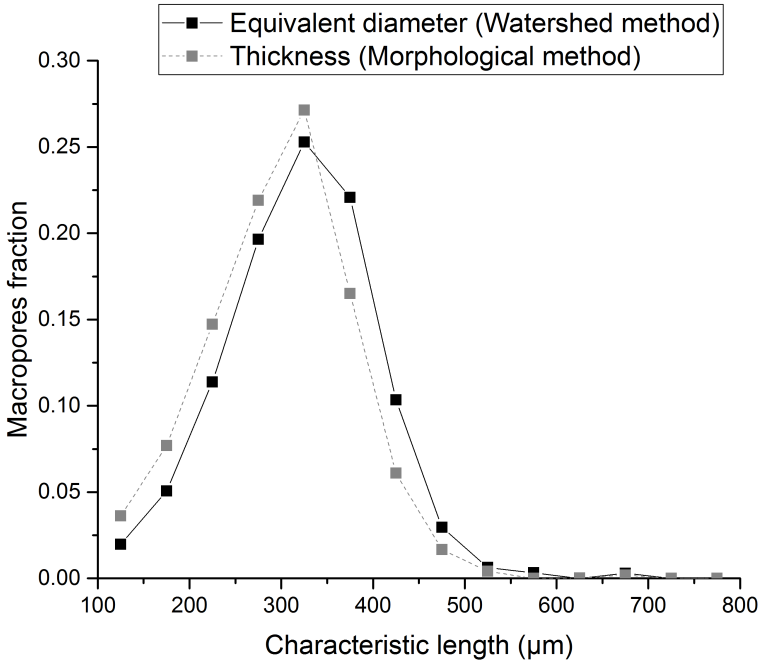

Figure 6: *Comparison of the two methods used to measure the size distribution of macroporosity for the reference formulation*

From all the scans performed at different resolutions and from the measurements of the total porosity, it is also possible to estimate the volume fraction of each type of porosity in our samples. For this, the fraction of macropores (air bubbles) from our 15 μm scans, is first determined on binary volumes. To do so, only pores with equivalent diameters larger than 100 μm were kept and their volume fraction computed. For the mesopores, 2 μm scans were used with their split mesopores and the pores with an equivalent diameter larger than 100 μm (already measured as the macroporosity) were removed. At this resolution, the volumes also contained small pores with equivalent diameter smaller than 10 μm. These were considered to belong to the micropores and were then also rejected. The fraction of the remaining pores was subsequently computed to get the mesopore fraction. Finally, microporosity was calculated as the difference between the total porosity (inferred from the macroscopic measurement of the density) and the sum of macro and mesoporosity fractions calculated from image processing as explained just above.

2.2.4 Spatial distribution of macropores

In order to characterize the spatial homogeneity of macroporosity, two criteria were applied on the 15 μm voxel scans, where only macropores are visible. The first one is a 2D criterion based on the minimum path algorithm [22]. This method is based on the Dijkstra algorithm which is commonly used to calculate the shortest path between two points. The principle is to consider that passing through the porous phase has no cost for the fracture unlike passing through gypsum phase which costs "energy" (stating that energy is a fixed density times the path length in that phase). The algorithm computes the cost of the minimum path that connects the two edges and goes by any given site. The Dijkstra algorithm can be used for "directed" paths (with no backtracking) or non-directed paths. In the latter case, the computation time is higher therefore "directed" paths were used in our case. Assessing this cost to the considered site produces the map shown in Figure 7b. Its cost is referred to as "minimum path cost". By calculating this cost for several slices and different orientations, the mean minimum path cost is obtained. If a pore cluster is present on the analyzed slice, the minimum path cost will be low because this pore cluster provides a low cost path. The minimum

path cost is hence sensitive to correlations in the spatial distribution of macropores (such as pore alignments).

Even though the minimum path can give us some information, it is only calculated on 2D images. Ideally, minimal surfaces in 3D would inform on the "cost" of a fracture surface through the microstructure. Algorithms exist to solve this problem [23], but their computation timr is much larger. In this study, we will limit ourselves to searching for a 1D path in a 3D volume. To do so, we used a 3D tortuosity Fiji inhouse plug-in. This method is also based on the Dijkstra algorithm. The main difference with the previously mentioned directed minimum path calculation is that the path may propagate in any direction. Besides, the porous network is percolating in 3D and the minimum cost is therefore zero for a 1D path, so we will rather focus on the length of the calculated path to characterize the different microstructures. In our case, one face of the volume is chosen as the starting plane. Every voxel from this face corresponding to the porous phase are gathered in a set list and the value zero is assigned to all of them. The minimal distance to go from the starting phase to every pores of the porous phase is calculated with the following method, described for the general case of any porous phase voxel. For one voxel in the set list, its 26 neighbors are examined. If they belong to the porous phase, the Euclidean distances between the starting voxel and the neighboring voxel are calculated. The addition of the value of the starting voxel and the Euclidian distance is the temporary value of the neighboring voxel. The voxel value is updated to the smallest of the temporary value coming from neighbors or the current value of the considered voxel. This principle is applied to all the voxels from the set list and every time a calculation is finished, the starting voxel is deleted from the set list and replaced by the neighbors whose value have been updated. The algorithm stops when the set list consists only of voxels belonging to the ending face of the volume. A map is finally obtained with each voxel in the 3D volume having the value of the minimum length of the path from the starting face. Figure 7c shows a slice of such a map in the reference sample. In this map, the darker the gray level in the porosity, the shorter the distance to the upper face. The ending face of such a volume contains a 2D map of the shortest distance between the starting and the ending face is then analyzed in order to calculate the mean path length (Fig. 7d). The mean value of the gray level in this face was calculated and then simply divided by the distance between the two faces to obtain the mean tortuosity.

For each type of sample, this calculation was made on three volumes for the six faces of the volume. 18 values for each formulation were obtained thereby, so that the mean value and the standard deviation of the tortuosity could be evaluated.

2.3 Mechanical characterization

The mechanical properties of every sample were measured by spherical indentation tests using an Electroforce EF 3200 test machine (Bose, Eden Prairie, MN). Load and displacement resolutions were 0.2 N and 1 μm,

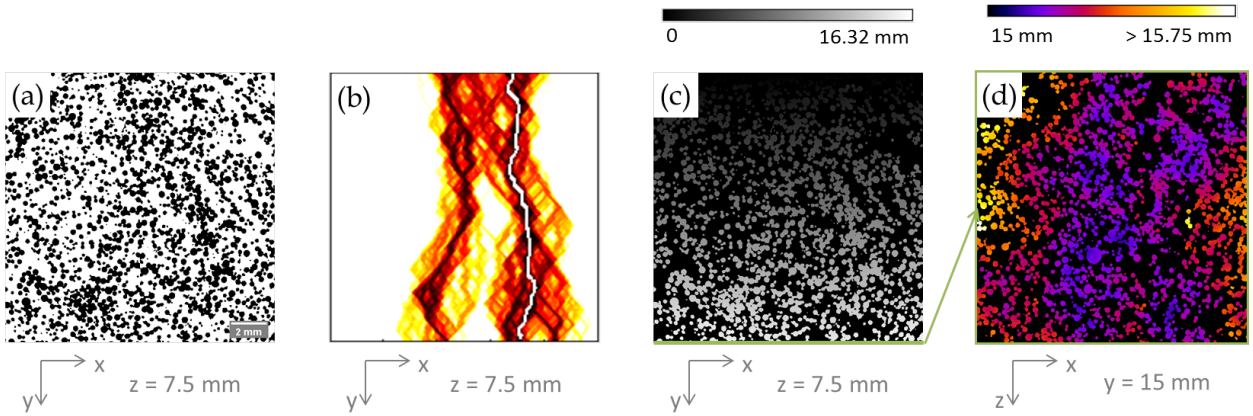

Figure 7: *Image processing to calculate homogeneity criteria a) binary volume slice with a 15 μm voxel size and porosity in black b) paths costs computed for one slice with minimum path cost in white c) map of minimum length of path going through each voxel from top face (i.e. minimum y) d) map of minimal length for the ending face (i.e. maximum y)*

respectively. Indentation tests were carried out using a tungsten carbide sphere of radius $r = 3$ mm. Six tests were conducted on two samples for each formulation. The analysis of load-displacement curves was made with the Oliver and Pharr method [24] to determine contact penetration and projected area of contact. This method is based on the hypothesis of a purely elastic unloading phase and it provides an estimate of the hardness without having to measure the contact area. This method has been validated by Clément *et al.* for highly porous brittle materials [25]. It allows the measurement of hardness and Young modulus from the displacement *vs* force curve. In this study, only hardness was measured because it is the most relevant parameter to represent the loading of the core of foamed gypsum boards.

3 Results and discussion

3.1 Fraction and size distribution of porosity

Figure 8 plots the obtained *vs* targeted overall density and table 3 shows the overall density and the fraction of each level of porosity for the 9 different types of samples used. These measurements were made for one sample per formulation. Macropore fraction was measured on 3 volumes of 3.4 cm^3 and mesopore fraction was measured on 3 volumes of 8 mm^3.

Table 3: *Distribution of the different levels of porosities for the three sets of parameters : board weight, water/plaster ratio and foam generator. The gray shaded line corresponds to the reference sample*

Designation	**Obtained density** ($\mathrm{g/cm}^3$)	**Macropore fraction**	**Mesopore fraction**	**Micropore fraction**	**Gypsum fraction**
REF	0.680	38%	9%	24%	29%
W70	0.535	46%	7%	24%	23%
W75	0.593	42%	9%	23%	26%
W80	0.645	41%	9%	22%	28%
W90	0.738	34%	9%	25%	32%
W100	0.795	29%	10%	27%	34%
R06	0.665	44%	9%	19%	29%
R08	0.665	33%	11%	27%	29%
DG	0.673	39%	8%	24%	29%

The obtained overall density is close to the targeted one and is successfully changed by modifying the foam fraction. The lightest and heaviest formulations (respectively W70 and W100) are slightly shifted with respect to the targeted densities (Fig. 8). In the case of W70, it is probably due to foam segregation. W70 is indeed a high foam fraction formulation with significant sensitivity to gravity. It is hence difficult to obtain the targeted density because of the variation of foam fraction in the slurry. In the case of W100 formulation, it is due to the manual introduction of foam into the slurry leading to uncertainty about the amount of introduced foam. Because W100 is a low foam fraction formulation, this relative uncertainty is larger than for other formulations.

When the foam fraction increases, the mesopore fraction decreases a bit if we compare the samples W70, REF and W100 (Table 3). This is not surprising because mesopores correspond to dissolved semi-hydrate particles and therefore their fraction decreases with the fraction of gypsum. Variations in the micropore fractions are too small to be taken into account because their measurements result from that of the other three parameters: density, macropore fraction and mesopore fraction and therefore accumulates measurement uncertainties.

To measure the influence of water/plaster ratio on the microstructure for a similar total density, the samples R06, REF and R08 can be compared. In order to keep the same density while changing the water/plaster ratio, the foam fraction has been changed: when the water/plaster ratio is increased, the foam fraction is decreased. It also has an impact on the micropore fraction which is higher for R08 and lower for R06 in

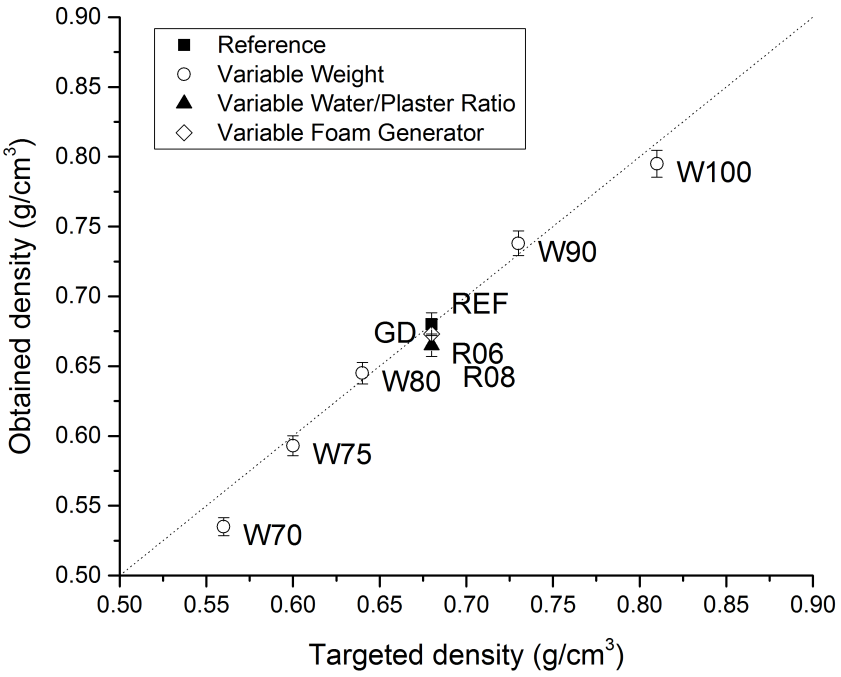

Figure 8: *Obtained vs targeted density for our 9 samples. The error bar corresponds to the density measurement uncertainty mostly due to difficulties in volume measurements. The dotted line corresponds to the $f(x)=x$ function*

comparison to the reference sample (Table 3). This is induced by an increase of water content into the slurry. When more water is evaporated, the amount of micropores increases. In order to verify this, tomography scans were made at high resolution (voxel size 0.3 μm) for the three formulations with a different water/plaster ratio as shown in Figure 9. It is quite complicated to measure the volume fraction of microporosity because even with this high resolution, gypsum needles are not visible and we don't have access to the whole microporosity. Microporosity fraction was measured on binarized volumes but the obtained values do not seem to be reliable: 20% for R06, 13% for REF and 16% for R08. However, a visual observation can still be made: a higher water/plaster ratio seems to produce more microporosity.

Because the type 2 generator produces smaller bubbles than the type 1 generator (see Fig. 10), the criterion for classifying macro and mesopores is set to 60 μm for the type 2 generator. Even with this different criterion, the fractions of macroporosity of the two generators are similar.

Volume fraction is not the only feature of porosity that we are interested in. The size distribution of pores may also impact the mechanical properties of foamed gypsum.

Figure 10 shows the size distribution of mesopores measured with 3D granulometry and the size distribution of macropores measured with the watershed algorithm. Changing the foam generator modifies the pore size distribution. Both generators gave a similar distribution of mesopores but the large mesopores produced by the type 2 generator were more numerous than for the type 1 generator as shown in Figure 10a. Concerning the macropores (Fig. 10b), all the formulations produced with the type 1 foam generator have the same size distribution with a mean value of equivalent diameter around 235 μm. The macropores diameters are found mainly in the 100 μm to 500 μm range. The type 2 foam generator produces smaller bubbles with a mean equivalent diameter of 117 μm and the macropores diameters are found mainly in the 60 μm to 400 μm range.

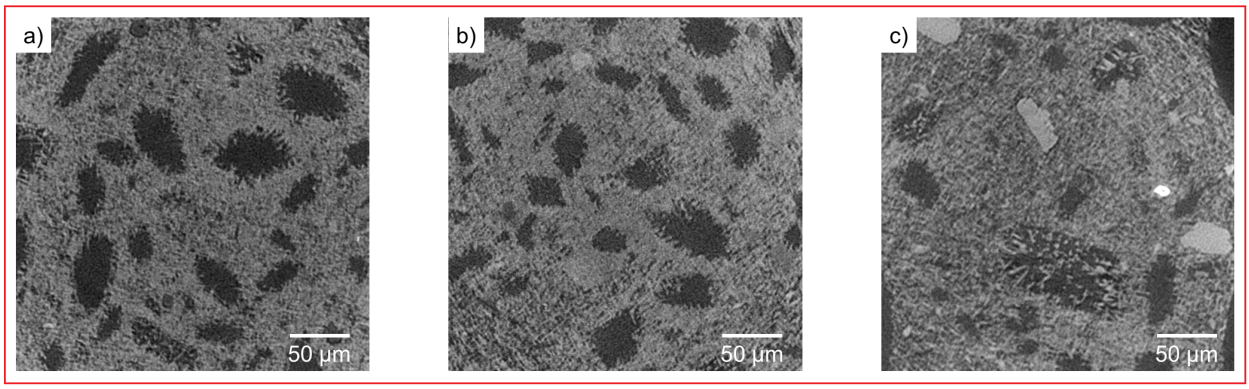

Figure 9: *Slice of tomography scan with a voxel size of 0.3 µm for a) R06 (W/P = 0.6) b) REF (W/P = 0.7) c) R08 (W/P = 0.8)*

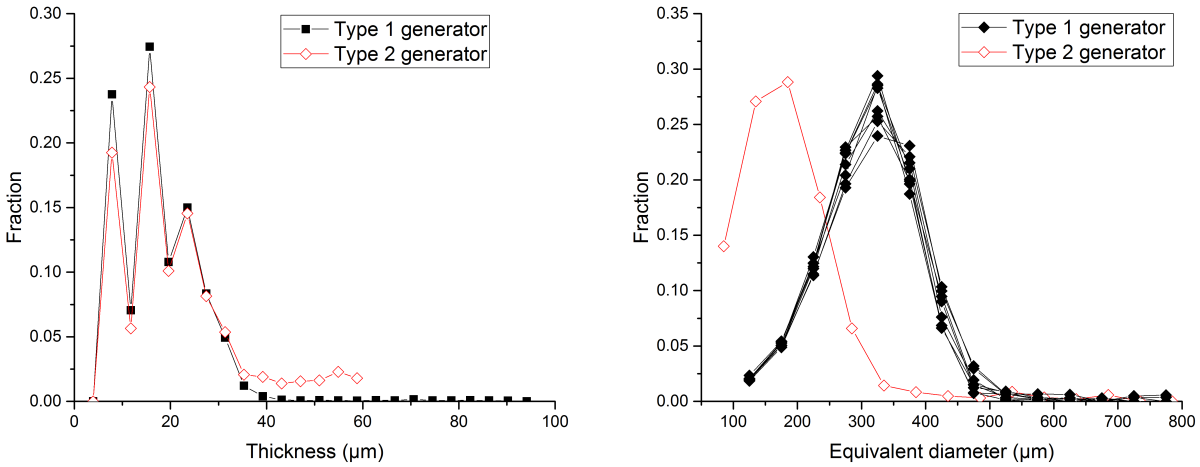

(a) *Thickness of mesoporous phase measured with 3D granulometry for REF and GD formulations on 2 µm voxel size scans*

(b) *Size distribution of macropores measured with watershed algorithm for all formulations on 5 µm voxel size scans*

Figure 10: *Analysis of size distribution of mesoporosity and macroporosity obtained with two different foam generators*

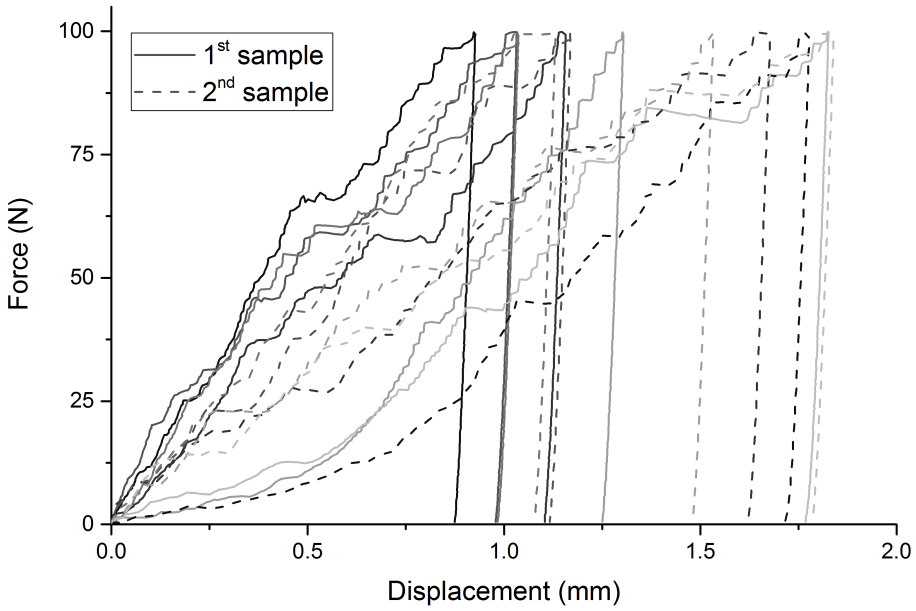

Figure 11: *Indentation curves obtained for two samples of the reference formulation, 6 tests have been conducted on each of the two different samples*

3.2 Link between microstructure and hardness

Spherical indentation tests have been conducted on all the 9 formulations. An example of the force *vs* displacement curves that were obtained for the reference formulation is shown in Figure 11. Six curves are shown for two different samples. Dispersion of maximal depth of indentation at 100 N is significant and so is the hardness dispersion. Thus error bars corresponding to standard deviation of hardness will be shown in Figures 12, 13, 14 and 15. The mean radius of contact at a maximum force of 100 N for the REF formulation is 2.5 mm which is about 15 times larger than the average radius of the macropores. This means that an area with a significant number of macropores is stressed during indentation and thus the effect of the three levels of porosity on hardness can be tested.

Hardness was obtained for every formulation at a maximum force of 100 N, with the exception of W70 samples which has been tested at 75 N maximum. The depth of indent into the lighter samples was indeed too large and became larger than the radius of the indentation ball, altering the result. Other indentation tests have been conducted with a maximum force of 30 N and the hardness obtained is roughly the same as with a 100 N but with a higher standard deviation. We therefore considered that the measurement of hardness with a 75 N maximum force can be compared to the one made with a 100 N maximum force.

3.2.1 Influence of density

Two samples have been tested for each formulation. As the density of each sample is slightly different, they have been plotted separately for the hardness *vs* density graph.

Figure 12 shows the hardness *vs* density curve for some of our formulations. It is well known that density affects the mechanical properties of porous materials [26] and it is visible in Figure 12. A trend curve was determined to describe the relationship between hardness and density. It corresponds to a power law according to the following equation (with H in MPa and ρ in $\mathrm{g/cm^3}$):

$$H = 13.08\ \rho^{2.41} \tag{1}$$

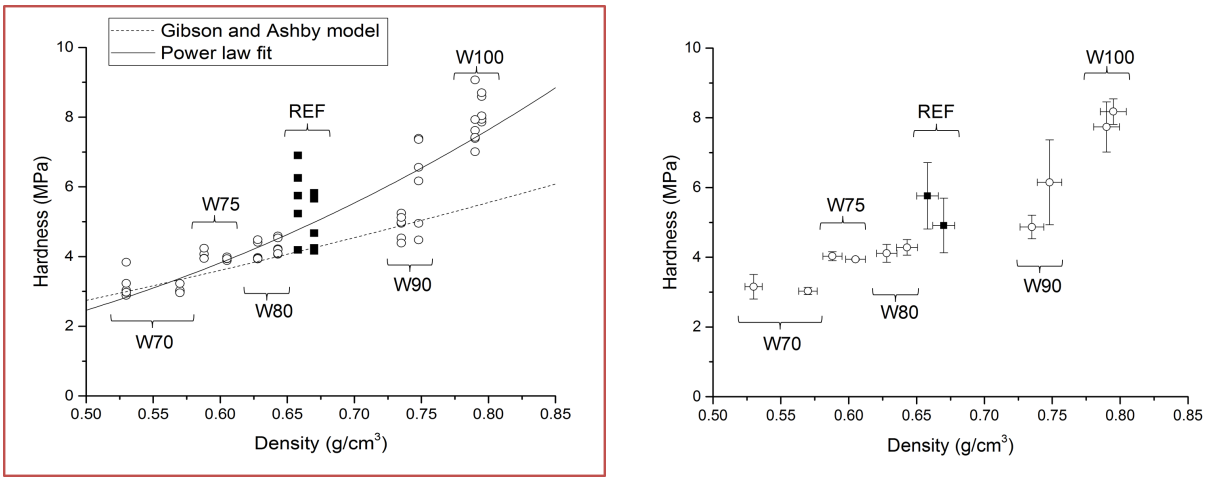

(a) (b)

Figure 12: *Relation between density and mechanical properties for formulations with density variation. a) All indentation results with the Gibson and Ashby prediction and the trend curve. b) Mean values of hardness for each sample*

It can be compared to the Gibson and Ashby model [26] for the crushing of brittle foams which corresponds to the equation 2 with σ^*_{cr} the crushing strength of the foam, σ_{fs} the strength of the solid ρ^* the density of the foam and ρ_s the density of the solid. The model applied to foamed gypsum gives the curve plotted in Figure 12a using Clement's data [25], *i.e.* a hardness of 40 MPa for a gypsum with a porosity of 56%.

$$\frac{\sigma^*_{cr}}{\sigma_{fs}} \approx 0.2 \left(\frac{\rho^*}{\rho_s}\right)^{3/2} \quad (2)$$

The overall trends of equations 1 and 2 are similar but the exponent of the observed trend is higher than for Gibson Ashby's model. However, it is difficult to compare them because the Gibson and Ashby model applies to cellular solids when our material is more a porous solid with different scales of porosity.

Although the equation 1 describes the general trend well, it can be noted that the samples W75 and W80 have similar mean values of hardness while their density are different. The same observation can be made for the samples REF and W90 in Figure 12b. This observation is very interesting from an industrial point of view because it means that the weight of a plate can be reduced by 0.5 $\mathrm{kg/m^2}$ while maintaining the same compression properties. It seems that another parameter than the density is affecting the hardness.

It can also be noted that the standard deviations of hardness are higher for the REF and W90 samples and to a lesser extent for the W100 sample. This corresponds to the formulations with the highest densities.

3.2.2 Effect of macroporosity

From previous studies such as [27], using *in situ* indentation tests on complete lightweight plasterboards, it is known that the main mechanism of damage is the collapse of macropores. Hence we are interested in studying the effect of the macropore fraction and size on hardness for similar densities. Figure 13 shows the effect of macropores size and fraction on the hardness. The size of macropores has been modified by changing the foam generator. However, it does not appear to affect the mechanical properties (Fig. 13a). It should be noted, however, that only the average value of the macropores diameter has been modified: the shape of the distribution curve is similar. It can therefore only be concluded that for this size distribution, the average size does not influence the hardness.

Moreover, the macropore fraction has been modified by varying the water/plaster ratio of the sample by keeping the same density but this change in porosity distribution does not affect the hardness either (Fig. 13b). This result should also be qualified because the change in the water/plaster ratio also has consequences

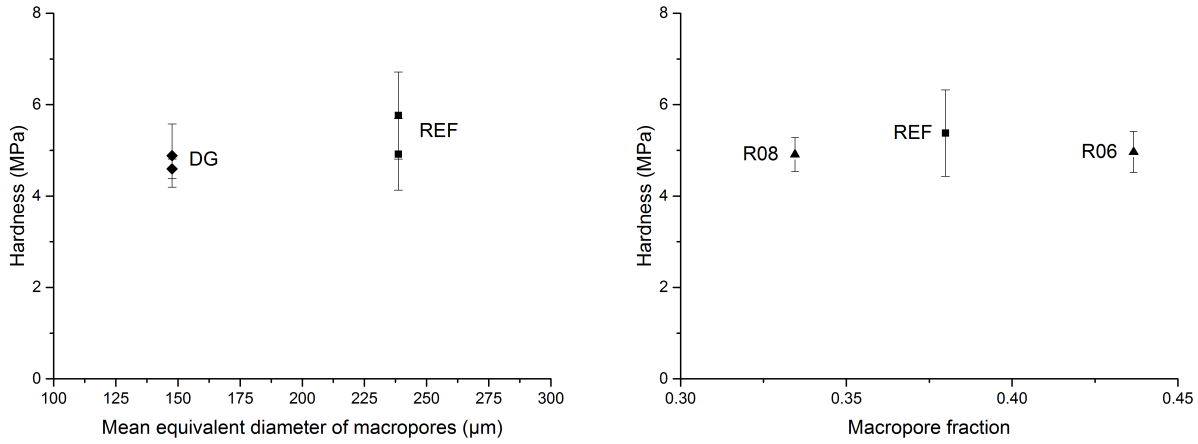

Figure 13: *Relation between mechanical properties and porosity distribution at same density a) by changing the mean equivalent diameter of macropores b) by changing the water/plaster ratio*

on the network of gypsum crystals. Water/plaster ratio does not have much influence on hardness when the density is similar.

3.2.3 Spatial homogeneity of macroporosity

In order to explain the hardness differences between samples with a similar density, the homogeneity of the microstructure in our samples was investigated at the macropore level. Spatial homogeneity of macroporosity is indeed crucial from a mechanical point of view. In the case of indentation, the material would collapse catastrophically if a group of macropores was present underneath the indentor. Thus the material has to be as homogeneous as possible, especially with regard to macropores. If the macropores are not distributed homogeneously, weak spots can appear in the foamed gypsum microstructure. If the mean porosity of the material has a significant role (as shown above), obviously the porosity in the small volume just beneath the indentor matters even much more, as it is the one that really dictates hardness. Hence, one would like to capture the variability of porosity at a very small scale. This involves the characterization of spatial correlation between pores. Various attempts were made to capture this small scale variability and the following analysis of minimum path and tortuosity were selected as the most sensitive ones. It is important to note that in terms of computation time, the 2D minimum directed path algorithm is much faster than the tortuosity (3D non-directed path) algorithm. Both calculations were computed on three volumes for each formulation and were associated to the two values of hardness for the mechanical tests. The mean value of hardness of the couple of samples is plotted for one value of tortuosity or minimum path cost.

The graphs in Figure 14 shows the hardness *vs* the minimum path cost (Fig. 14a) and the tortuosity (Fig. 14b) for the formulations with density variation. Even though the trend of a linear relation between hardness and the minimum path cost seems to exist when density is varying, samples having the same hardness do not have the same minimum path cost (Fig. 14a). It is for example the case for the two couples of formulations W90-REF and W80-W75.

As for the minimum path, there is a good correlation between hardness and tortuosity (Fig. 14b). Moreover the couple of formulations W75 and W80 have similar hardness values and similar tortuosity values. However, the tortuosity values are not totally in agreement with the hardness values, especially for formulations with a variation in the water/plaster ratio. Moreover, for low tortuosity values, there is no correlation between hardness and tortuosity.

Minimum path cost and tortuosity were first thought to be sensitive to heterogeneity and pore clusters in our volume, which are crucial from a mechanical point of view. However, if they are sensitive to heterogeneity, they are also sensitive to macropore fraction. For a formulation with a higher foam fraction, it is obvious that

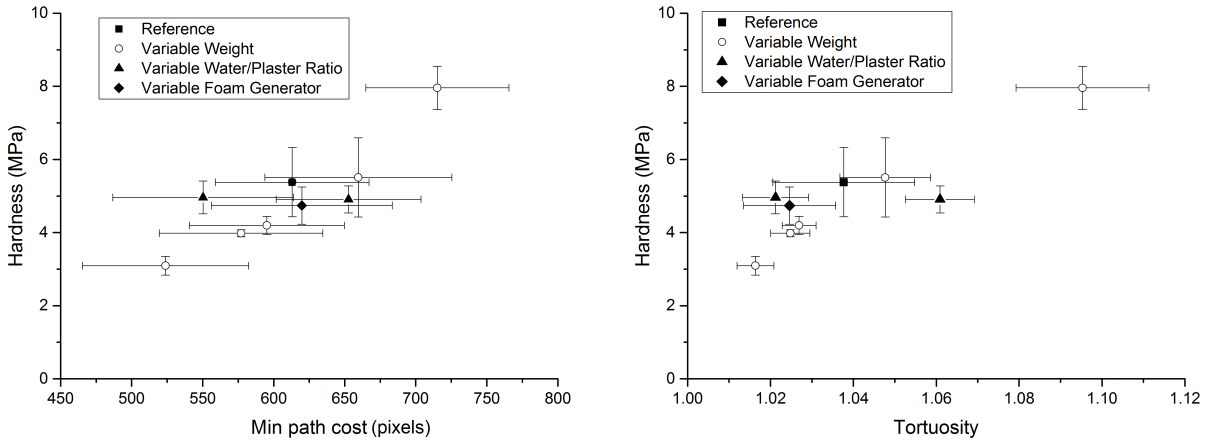

(a) (b)

Figure 14: *Relation between hardness and a) minimum path cost b) tortuosity*

there will be more chances to find a path with a smaller cost between two sides and more chances to find a straight path through macropores.

Figure 15 shows the relation between the two criteria of homogeneity and (Fig. 15a) and hardness (Fig. 15b) with macropore fraction. Minimum path cost and tortuosity are strongly related to the macroporosity fraction. A linear relation with a negative slope links minimum path and macropore fraction. Tortuosity is also related to the macropore fraction but for high macropore fractions (above 40%, see Figure 15a) tortuosity tends to the asymptotic value of 1, thereby loosing sensitivity. In this limit, tortuosity is then less sensitive to the spatial distribution of macropores.

Hardness is also strongly related to the macropore fraction (Fig. 15b). The only formulations that do not follow this trend are those for which we have varied the water/plaster ratio.

Minimum path cost and tortuosity are therefore not deterministic indications of hardness but there is a clear trend that links these parameters to average hardness as well as macropore fraction (Fig. 15).

The standard deviation of hardness was greater for formulations with high densities: REF, W90 and W100 as reported above. For a formulation with a low macropore fraction, the volume fraction of the macropores may vary significantly in the indented area. On the contrary, for a formulation with a large fraction of macropores, the indented area will always encounter many macropores and thus will display less fluctuations.

The graph in Figure 16 shows the relation between the standard deviation of hardness *vs* the standard deviation of tortuosity. We can see that the dispersion of tortuosity is related to the dispersion of hardness measurements, with the exception of W90 which has a high standard deviation of hardness from the overall trend. Thus standard deviation of tortuosity over several measurements, provides information on the spatial distribution of macropores and its impact on mechanical properties in indentation.

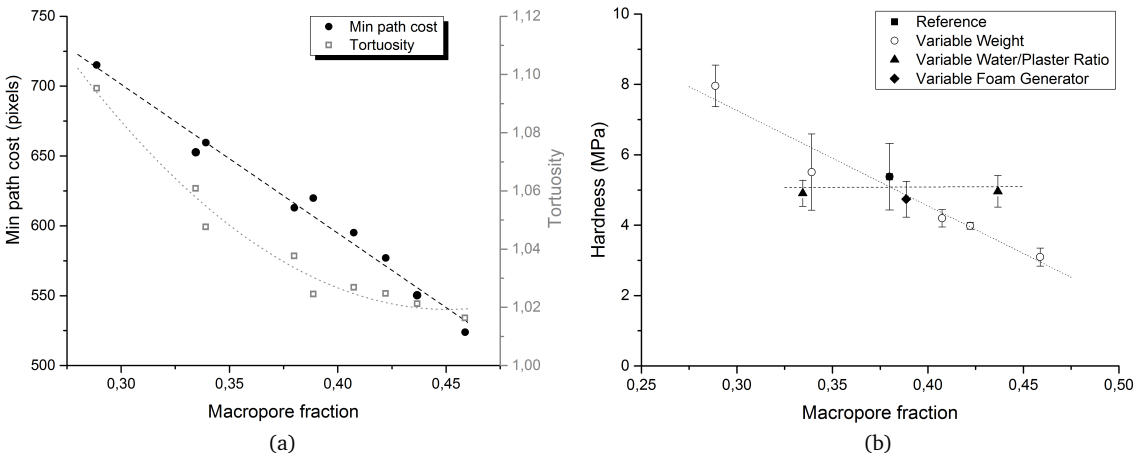

Figure 15: *a) Relation between macropore fraction and the two criteria of homogeneity. The dotted line and the dashed line represent the respective trend curves of tortuosity and minimum path cost . b) Relation between macropore fraction and hardness. The dotted line and the dashed line represent the respective trend curves for the variable weight samples and the variable water/plaster ratio samples.*

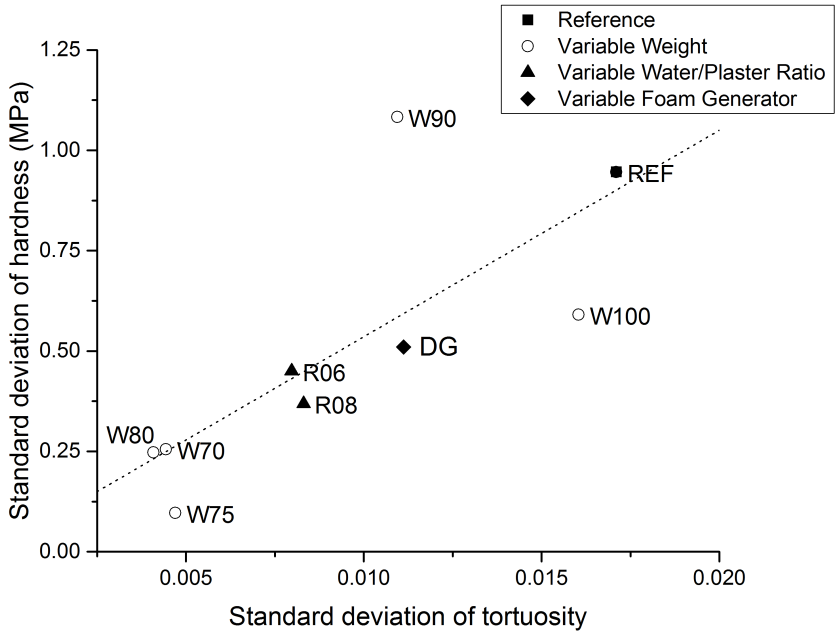

Figure 16: *Relation between standard deviation of tortuosity and standard deviation of hardness*

4 Conclusion and prospects

We have linked the microstructure features, analyzed by 3D imaging, with the mechanical properties, measured by spherical indentation tests, for a broad range of foamed gypsum formulations.

Methods of thresholding and microstructure characterization by image processing were developed to treat specifically the tri-modal porosity observed in our tomography scans. This resulted in a very detailed analysis of the microstructure of the 9 different types of formulations used in this study. The different image processing methods enabled the precise measurement of each type of porosity and of the size distribution of the macro and meso pores. The density was tuned by adjusting the rate of foam incorporated in the batch, the distribution of the three levels of porosity varied by modifying the water/plaster ratio to the same density and the average macropore size decreased by changing the foam generator.

Thanks to controlled microstructures, the connection between microstructure features and hardness were highlighted. As expected, density was shown to have a great influence on hardness. The macroporosity fraction is also of primary importance for the hardness as measured in indentation. In contrast, macropore size has no influence on hardness but this study was limited only to comparing two monomodal distributions with a different mean size. It would be interesting to study the impact of a bimodal distribution of macropores or to work at different densities to further investigate the influence of the macropore size distribution on hardness and also on other mechanical properties.

The spatial homogeneity of the macropores, was also quantified and was found to have a major role in the mean value and the dispersion of measured hardness.The heterogeneity and thus the hardness dispersion was more important for formulations with a low foam fraction. This scatter in the hardness measurement of the high density foams could finally be linked with scatter of the measured tortuosity, indicating that this latter parameter is possibly a good descriptor to infer the distribution of the hardness measurement.

Acknowledgments

The authors wish to thank Saint-Gobain Research Paris for supporting this research project, and particularly Xavier Brajer and Chrisitne Nguyen. Julie Devillard is also financially supported by ANRT through contract no. 2018/1219.

References

[1] I. Soroka and P. J. Sereda. Interrelation of hardness, modulus of elasticity, and porosity in various gypsum systems. *Journal of the American Ceramic Society*, 51(6):337–340, 1968.

[2] D. Jeulin, P. Monnaie, and F. Péronnet. Gypsum morphological analysis and modeling. *Cement and Concrete Composites*, 23(2):299–311, 2001.

[3] S. Meille, M. Saâdaoui, P. Reynaud, and G. Fantozzi. Mechanisms of crack propagation in dry plaster. *Journal of the European Ceramic Society*, 23(16):3105–3112, 2003.

[4] J. Sanahuja, L. Dormieux, S. Meille, C. Hellmich, and A. Fritsch. Micromechanical explanation of elasticity and strength of gypsum: From elongated anisotropic crystals to isotropic porous polycrystals. *Journal of Engineering Mechanics*, 136(2):239–253, 2010.

[5] Q. L. Yu and H. J. H. Brouwers. Microstructure and mechanical properties of beta-hemihydrate produced gypsum: An insight from its hydration process. *Construction and Building Materials*, 25(7):3149–3157, 2011.

[6] N. Payraudeau Le Roux, S. Meille, J. Chevalier, E. Maire, and J. Adrien. In situ observation of plaster microstructure evolution during thermal loading. *Fire and Materials*, 40(7):973–984, 2016.

[7] P. Keerthan and M. Mahendran. Numerical studies of gypsum plasterboard panels under standard fire conditions. *Fire Safety Journal*, 53:105–119, 2012.

[8] Astm standard c473-07 standard test methods for physical testing of gypsum panel products. www.astm.org, 2007.

[9] A. Bouterf, J. Adrien, E. Maire, X. Brajer, F. Hild, and S. Roux. Failure mechanisms of plasterboard in nail pull test determined by x-ray microtomography and digital volume correlation. *Experimental Mechanics*, 56(8):1427–1437, 2016.

[10] J. Adrien, S. Meille, S. Tadier, E. Maire, and L. Sasaki. In-situ x-ray tomographic monitoring of gypsum plaster setting. *Cement and Concrete Research*, 82:107–116, 2016.

[11] E. Maire and P. J. Withers. Quantitative x-ray tomography. *International materials reviews*, 59(1):1–43, 2014.

[12] A. Çolak. Density and strength characteristics of foamed gypsum. *Cement and Concrete Composites*, 22(3):193–200, 2000.

[13] A. Vimmrová, M. Keppert, L. Svoboda, and R. Černý. Lightweight gypsum composites: Design strategies for multi-functionality. *Cement and Concrete Composites*, 33(1):84–89, 2011.

[14] J.-Y. Buffiere, E. Maire, J. Adrien, J.-P. Masse, and E. Boller. In situ experiments with x ray tomography: an attractive tool for experimental mechanics. *Experimental Mechanics*, 50(3):289–305, 2010.

[15] J. Schindelin, I. Arganda-Carreras, E. Frise, V. Kaynig, M. Longair, T. Pietzsch, S. Preibisch, C. Rueden, S. Saalfeld, B. Schmid, J.-Y. Tinevez, D. J. White, V. Hartenstein, K. Eliceiri, P. Tomancak, and A. Cardona. Fiji: an open-source platform for biological-image analysis. *Nature Methods*, 9:676, 2012.

[16] C. H. Li and P. K. S. Tam. An iterative algorithm for minimum cross entropy thresholding. *Pattern Recognition Letters*, 19(8):771–776, 1998.

[17] N. Phansalkar, S. More, A. Sabale, and M. Joshi. Adaptive local thresholding for detection of nuclei in diversity stained cytology images. In *2011 International Conference on Communications and Signal Processing*, pages 218–220.

[18] B. Münch, P. Gasser, L. Holzer, and R. Flatt. Fib-nanotomography of particulate systems—part ii: Particle recognition and effect of boundary truncation. *Journal of the American Ceramic Society*, 89(8):2586–2595, 2006.

[19] T. Thiede, T. Mishurova, S. Evsevleev, I. Serrano-Munoz, C. Gollwitzer, and G. Bruno. 3d shape analysis of powder for laser beam melting by synchrotron x-ray ct. *Quantum Beam Science*, 3(1):3, 2019.

[20] J. Ollion, J. Cochennec, F. Loll, C. Escudé, and T. Boudier. Tango: a generic tool for high-throughput 3d image analysis for studying nuclear organization. *Bioinformatics*, 29(14):1840–1841, 2013.

[21] T. Hildebrand and P. Rüegsegger. A new method for the model independent assessment of thickness in three dimensional images. *Journal of Microscopy*, 185(1):67–75, 1997.

[22] S. Roux and D. François. A simple model for ductile fracture of porous materials. *Scripta Metallurgica et Materialia*, 25(5):1087–1092, 1991.

[23] Y. Boykov and V. Kolmogorov. Computing geodesics and minimal surfaces via graph cuts. In *Proceedings Ninth IEEE International Conference on Computer Vision*, pages 26–33 vol.1.

[24] W. C. Oliver and G. M. Pharr. An improved technique for determining hardness and elastic modulus using load and displacement sensing indentation experiments. *Journal of Materials Research*, 7(6):1564–1583, 1992.

[25] P. Clement, S. Meille, J. Chevalier, and C. Olagnon. Mechanical characterization of highly porous inorganic solids materials by instrumented micro-indentation. *Acta Materialia*, 61(18):6649–6660, 2013.

[26] L. J. Gibson and M. F. Ashby. *Cellular solids: structure and properties*. Cambridge university press, 1999.

[27] A. Bouterf, E. Maire, S. Roux, F. Hild, X. Brajer, E. Gouillart, and E. Boller. Analysis of compaction in brittle foam with multiscale indentation tests. *Mechanics of Materials*, 118:22–30, 2018.